Lab on a Chip

Disposable photonics for cost-effective clinical bioassays: application to COVID-19 antibody testing

Journal:	*Lab on a Chip*
Manuscript ID	LC-ART-04-2021-000369.R1
Article Type:	Paper
Date Submitted by the Author:	28-May-2021

Complete List of Authors:	Cognetti, John; University of Rochester, Biomedical Engineering Steiner, Daniel; University of Rochester, Biochemistry and Biophysics Abedin, Minhaz; SUNY Polytechnic Institute - Albany Campus, College of Nanoscale Science and Engineering Bryan, Michael; University of Rochester, Biochemistry and Biophysics Shanahan, Conor; University of Rochester, Biomedical Engineering Tokranova, NAtalia; SUNY Polytechnic Institute Young, Ethan; Ortho-Clinical Diagnostics Inc Research Headquarters Klose, Alanna; University of Rochester, Dermatology Zavriyev, Alexander; University of Rochester, Dermatology Judy, Nicholas; University of California Santa Barbara Piorek, Brian; University of California - Santa Barbara, Institute of Collaborative Biotechnologies; Numerical Design, Inc., Meinhart, Carl; University of California, Santa Barbara, Department of Mechanical Engineering Jakubowicz, Raymond; Ortho-Clinical Diagnostics Inc Research Headquarters Warren, Harold; Ortho-Clinical Diagnostics Inc Research Headquarters Cady, Nathaniel; SUNY Polytechnic Institute, Colleges of Nanoscale Science & Engineering Miller, Benjamin; University of Rochester, Dermatology

ARTICLE

Received 00th January 20xx,
Accepted 00th January 20xx
DOI: 10.1039/x0xx00000x

Disposable photonics for cost-effective clinical bioassays: application to COVID-19 antibody testing

John S. Cognetti,[a‡] Daniel J. Steiner,[b‡] Minhaz Abedin,[c‡] Michael R. Bryan,[b‡] Conor Shanahan,[a] Natalya Tokranova,[c] Ethan Young,[d] Alanna M. Klose,[g] Alexander Zavriyev,[e] Nicholas Judy,[f] Brian Piorek,[f] Carl Meinhart,[f] Raymond Jakubowicz,[d] Harold Warren,[d] Nathaniel C. Cady,[c] Benjamin L. Miller[a,b,e,g,*]

Decades of research have shown that biosensors using photonic circuits fabricated using CMOS processes can be highly sensitive, selective, and quantitative. Unfortunately, the cost of these sensors combined with the complexity of sample handling systems has limited use of such sensors in clinical diagnostics. We present a new "disposable photonics" sensor platform in which rice-sized (1 x 4 mm) silicon nitride ring resonator sensor chips are paired with plastic micropillar fluidic cards for sample handling and optical detection. We demonstrate the utility of the platform in the context of detecting human antibodies to SARS-CoV-2, both in convalescent COVID-19 patients and for subjects undergoing vaccination. Given its ability to provide quantitative data on human samples in a simple, low-cost single-use format, we anticipate that this platform will find broad utility in clinical diagnostics for a broad range of assays.

Introduction

Photonic sensors fabricated using processes amenable to standard silicon foundry (CMOS) workflows have proven to be exceptional tools for detecting biological molecules. Salient examples of photonic integrated circuits (PICs) used for sensing and produced either in silicon-on-insulator or silicon nitride include Mach-Zehnder interferometers,[1,2] ring resonators,[3,4] and photonic crystals.[5,6,7,8] While all have demonstrated utility in detecting and quantifying biomolecules in human samples, a challenge for the field in the context of diagnostics is to implement photonic sensors in a format that is inexpensive, easy to use, and fast. A photonic sensor's cost is driven by its size and by the number of mask levels required for its production, which in turn is a function of its level of integration. Much current effort in the sensing field is focused on increasing integration, up to fully monolithic sensing structures with the source (laser), detection element, and spectrometer on-chip.[9] This is a worthy goal, but there is also a significant need for research towards sensor formats that minimize cost while still providing the advantages of photonic sensors (sensitivity, multiplex capability, and potential for label-free/reagentless operation).

In the context of an overall program focused on the development of scalable manufacturing strategies for photonic sensors as part of the mission of AIM Photonics, we initiated the design and testing of sensor formats suitable for low-cost, high-throughput analysis of clinical specimens. To minimize the area of the sensor itself, while simplifying handling and sample delivery, we combined a small (1 x 4 mm) sensor incorporating ring resonators fabricated in silicon nitride with a plastic card featuring micropillar microfluidics. This allows the entire assembly to be produced at low cost, providing a single-use disposable assay. This assay consumable is paired with an optical hub design enabling rapid alignment of optical I/O on the sensor PIC via grating couplers (Figure 1).

The "disposable photonics" sensor format is a platform technology suitable for application to a broad range of diagnostic tests. To satisfy an existing clinical need and provide an initial demonstration of the format, we tested it in the context of detecting antibodies to SARS-CoV-2 antigens in human serum. SARS-CoV-2, the coronavirus responsible for the COVID-19 pandemic, at this point needs no introduction. Onset of the pandemic in February 2020 led to the rapid development of a large number of antibody testing formats,[10] including platforms using silicon ring resonators.[11] However, rapid assays able to provide quantitative readouts with an ability to scale to multiplex analyses remain lacking. Several mutant strains of SARS-CoV-2 have already arisen, and are cause for concern. Thus, antibody tests able to assess vaccine response with scalability to analyzing antibody affinity to multiple mutant strains of virus is also important. Here, we demonstrate use of the platform for detection of anti-SARS-CoV-2 antibodies in human serum samples from convalescent COVID-19 patients and vaccinated subjects. Two domains of the SARS-CoV-2 spike protein, S1+S2 and RBD (receptor binding domain) were used as antigens in the assay.

Methods

Materials

Recombinantly expressed (baculovirus) SARS-CoV-2 Spike protein domains (S1+S2 and RBD) and anti-spike monoclonal

Departments of [a]Biomedical Engineering, [b]Biochemistry and Biophysics, [e]Optics, and [g]Dermatology, University of Rochester, Rochester, New York
[c]College of Nanoscale Science and Engineering, SUNY Polytechnic, Albany, New York
[f]Department of Mechanical Engineering, University of California at Santa Barbara, Santa Barbara, California
[d]Ortho-Clinical Diagnostics, Rochester, New York
[‡]These authors contributed equally to this work
*Corresponding Author: Benjamin_miller@urmc.rochester.edu
Electronic Supplementary Information (ESI) available: Supplementary videos V1-V3 of fluid flow in micropillar microfluidic channels. See DOI: 10.1039/x0xx00000x

antibodies were obtained from Sino Biological, Inc. (Wayne, PA). Anti-fluorescein (anti-FITC) antibody used as a nonspecific binding control was obtained from Rockland Immunochemicals (Limerick, PA). The diluent for antibody/antigen printing was modified (i.e., potassium-free) phosphate-buffered saline (mPBS). Assay wash buffer (AWB), which was used to dilute serum samples, consists of mPBS with 3 mM EDTA and .01% Tween-20. All serum samples were diluted 1:5 in AWB. Pooled normal human serum (PNHS) was purchased (Innovative Research, Novi, MI) and also diluted 1:5 in AWB for use as a block for nonspecific binding, as well as a refractive index-matching fluid to prep the device for assaying each serum sample. ACS reagent-grade toluene (Fisher) was distilled over sodium metal immediately prior to use.

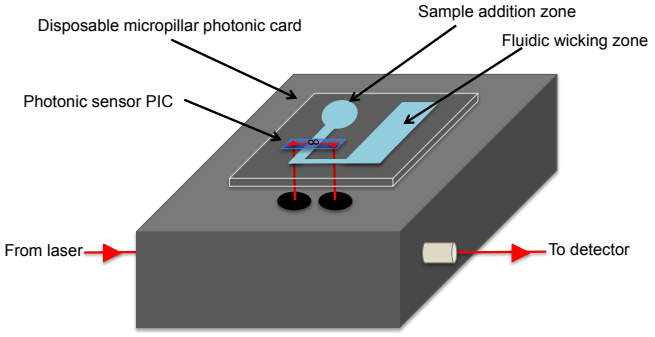

Figure 1. Overall concept: A small ring resonator photonic sensor (PIC) is integrated with a plastic micropillar microfluidics card. Interrogation of the sensor is accomplished using an optical hub co-designed with the PIC.

Serum samples were obtained from convalescent COVID-19 patients via the University of Rochester Medical Center healthy donor protocol. All subjects were at least 14 days out of active disease. Samples from vaccination subjects were obtained under a separate protocol approved by the University of Rochester Medical Center Institutional Review Board. All subjects were at least 18 years of age at the time of blood draw, and subject to informed consent.

Whole blood samples were allowed to clot for 30 minutes after draw. Samples were then spun at 1200×*g* for 5 mins, and serum was pipetted off into a 15 mL conical tube and spun again for 10 minutes to remove any remaining cellular material. The serum was then aliquoted and stored at -80 °C until use.

Ring resonators

Silicon nitride ring resonators were designed with an upper aqueous cladding for use in biosensing. The ring resonators studied in this work consist of silicon nitride waveguides 1.5 µm wide and 220 nm tall, supporting a single transverse electric (TE) polarization mode. Modeling was performed using the finite difference (FD) method in OptoDesigner, a component of the Synopsys Photonic Design Suite.

A cross-section of the layer stack as modeled is shown in Figure 2(a). The silicon nitride waveguide is insulated from the bulk silicon wafer by a bottom oxide layer 5 µm thick. An additional ~4 µm of top oxide cladding is added to isolate the waveguide from the environment. This isolation is critical to the performance of the grating couplers, the design of which is discussed further below. Near the ring resonators, the top oxide cladding is removed to enable sensing by exposing the waveguide to the analyte. The effective index of the guided mode, and the substrate and bending losses, were estimated through modeling (Figure 2(b) and (c)). Critical coupling of ring resonators is obtained by matching the coupling strength to the round-trip loss of the ring. Sensor PICs were designed to have two rings with slightly different diameters on a single bus waveguide in order to provide resonance signals at two different wavelengths. In experiments detailed below, one ring was designated as the experimental, and one as reference. PICs were also fabricated with three rings along one bus waveguide, in which one of the three rings was left un-exposed to the environment (i.e., under top oxide) to be used as a thermal

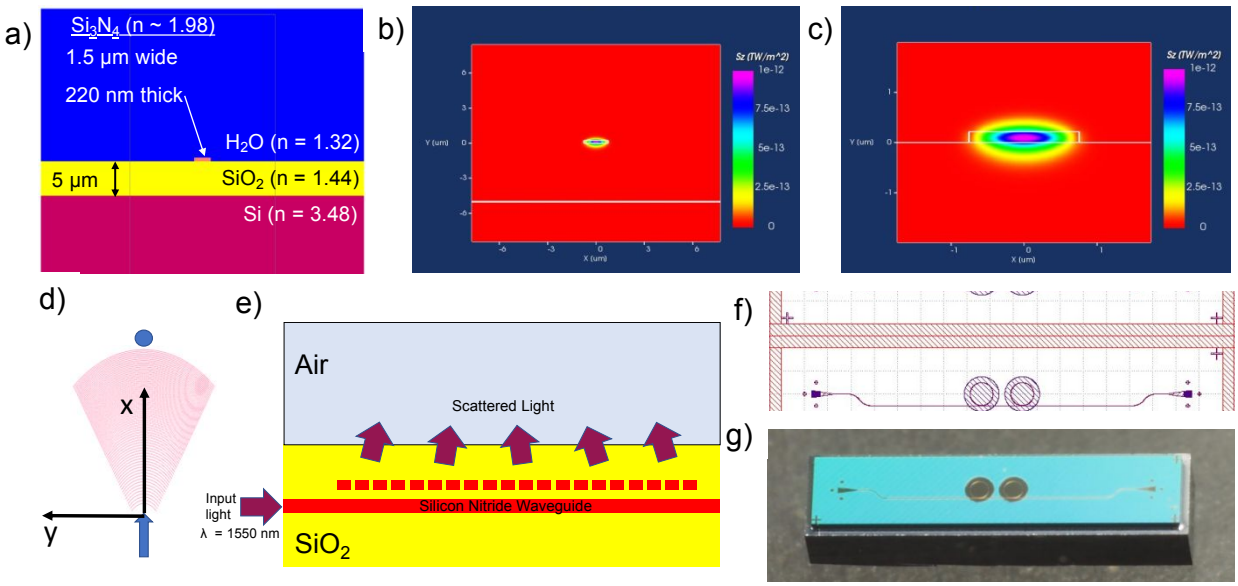

Figure 2: (a) Cross-section of silicon nitride waveguide used in modeling. (b), (c) Contour plots showing the full simulated structure (b) and waveguide close-up (c) for electric field distribution of fundamental TE mode; (d) Coordinate system for the focus grating couplers; (e) Geometry for the silicon-nitride focus-grating couplers; (f) GDS layout for 1 x 4 mm PIC with two ring resonators exposed to the environment; (g) Image of a single fabricated 1 x 4 mm sensor PIC.

control. We found that, given the internal referencing of the experimental ring to the nonspecific binding control, this additional control was not necessary, and so all experimental data discussed below uses the two-ring PICs.

Grating coupler design

The AIM Photonics layer stack includes two nitride layers. Focus-grating couplers are formed by patterning a grating in the top nitride layer, which perturbs λ_0 = 1550 nm light propagating in the lower nitride waveguide, as shown in Figure 2(e). Offsetting the grating from the waveguide allows for a weaker grating so that photons can be scattered (or collected) over a relatively large aperture. The grating spacing is determined from the phase-matching condition

$$\boldsymbol{n_m}\left[\boldsymbol{f_x^2}+\boldsymbol{f_y^2}+\boldsymbol{f_z^2}\right]^{\frac{1}{2}}+\boldsymbol{m\lambda_0}=\boldsymbol{n_{eff}}\left[\boldsymbol{x^2}+\boldsymbol{y^2}\right]^{\frac{1}{2}}+\boldsymbol{n_m}\left[(\boldsymbol{f_x}-\boldsymbol{x})^2+(\boldsymbol{f_y}-\boldsymbol{y})^2+\boldsymbol{f_z^2}\right]^{\frac{1}{2}}, \quad (1)$$

where, f_x, f_y and f_x indicate the focus point relative to the origin of the grating (Figure 2(d)), x and y are the in-plane coordinates of the gratings, n_m is the index of the surrounding medium, and n_{eff} is the effective index of the grating.[12,13] The index *m* represents the grating number.

COMSOL Multiphysics software was used to simulate the Helmholtz equation for the electromagnetic field in the symmetric *x-z* plane. The simulations provide insight for the grating strength, number of grating structures, and suitable apodization. Once the basic *x-z* plane grating was designed in COMSOL, a custom MATLAB algorithm was used to calculate the full *x-y* plane grating structure by solving Eq. (1). The results were then written to a GDS file for integration into the PIC, an overall GDS file for which is shown in Figure 2(f).

Photonic Chip Fabrication

Photonic sensors were fabricated in a custom run format using the 300 mm AIM Photonics fabrication line[14] with modifications to the standard AIM passive multi-project wafer (MPW) process and layer stack described above. A fabricated PIC is shown in Figure 2(g).

Micropillar Array Design and Fabrication

PICs were integrated with an inexpensive microfluidic card designed to provide passive flow of sample liquids to the photonic chip for analysis. For precise control of analyte delivery, the microfluidic card requires a sample introduction zone, channels to direct fluid flow, a detection zone where the PIC chip comes in contact with fluid, and a wicking zone to serve as a fluid sink and enhance flow through capillary or evaporative action. A schematic of the microfluidic card used in this work is shown in Figure 3(a). To achieve fluid flow without the need for external pressure-driven pumping or complex fluid control systems, a micropillar-based capillary flow approach was utilized in the microfluidic card design. Many simulation studies have demonstrated the potential for controlling fluid flow in micropillar capillary flow systems[15,16,17,18] and these approaches have been put into practice for a variety of biological assays and flow applications.[19,20,21] As far as we are aware, however, our work represents the first example of the integration of a photonic sensor with passive micropillar microfluidics. The pillars inside the channels serve as passive elements to provide the fluid transport and deliver analyte to the detection zone. By analogy to disposable micropillar analysis cards described previously,[22,23] polymer-based fabrication approaches were used, as they offer a significant cost savings and enable high volume manufacturing.

The process of polymer microfluidic card fabrication involved four major steps:1) silicon mold microfabrication, 2) hot embossing into polymer, 3) drilling alignment and optical input/output ports, and 4) integration of the PIC chip. To fabricate the mold, a photomask with the card design was created in Mentor Tanner L-Edit, then transferred onto an 8" (200 mm) silicon wafer using photolithography. During the photolithography step, a 5 µm layer of the photoresist MEGAPOSIT SPR™ 220-4.5 was patterned, followed by etching to 80 µm depth using DRIE in a Plasmatherm Versalock etching tool using SF_6 as the etching gas and C_4F_8 as the deposition gas. Deep reactive ion etching (DRIE) was then used to form the three-dimensional mold structure in silicon.

After the silicon mold was prepared, it was placed together with a polymer substrate (Zeonor cyclic olefin copolymer, 1 mm starting thickness) into a hot embossing system that includes a vacuum chamber and two heated plates (EVG 501 Wafer Bonder). Zeonor and the silicon mold were heated to above the polymer glass transition temperature (145 ºC) under 5 mTorr vacuum and pressed together by applying 3 kN force for 20 minutes. Subsequently, the materials were kept under applied force and cooled down to the room temperature to prevent deformation due to cooling. The silicon mold was dissolved in a mixture of hydrofluoric and nitric acids to release the microfluidic cards. An image of the completed micropillar microfluidic card is shown in Figure 3(b), with SEM images of pillars near the detection area in Figures 3(d) and 3(e).

Photonic Sensor Chip Functionalization

Following fabrication, 300 mm wafers were diced, and returned to us on dicing tape. Prior to functionalization, sensor PICs were removed from the dicing tape and first washed for 30 minutes in a 1:1 mixture of methanol and concentrated hydrochloric acid, then rinsed 3 x 30 seconds in Nanopure water and dried with nitrogen. PICs were next submerged in 1% (3-triethoxysilyl)propylsuccinic anhydride (Gelest, Morrisville, PA) in anhydrous toluene at ambient temperature for 40 minutes, and then rinsed in pure anhydrous toluene for 5 minutes. PICs were then dried with nitrogen, and heated at 110 °C for 30 minutes in an oven to stabilize the silane layer.

Antigens and control antibodies were covalently attached to the functionalized surface by spotting them directly on the rings using a sciFLEXARRAYER SX piezoelectric microarrayer (Scienion AG, Berlin, Germany). The control ring was spotted with anti-FITC antibody at 650 µg/mL in mPBS (pH 5.8), and the test ring with SARS-CoV-2 receptor-binding domain (RBD) peptide at 400 µg/mL in mPBS (pH 7.2), or S1 + S2 domain at 400 µg/mL in mPBS (pH 7.2). Both rings received approximately 3 nL of antibody/antigen solution. Chips were maintained at 75% humidity for 30 minutes, then overspotted with an equivalent volume of stabilizer solution (StabilCoat Immunoassay Stabilizer, Surmodics IVD Inc., Eden Prairie, MN). 30 minutes after stabilizer was spotted onto the rings, PICs were removed from the arrayer and kept in a vacuum desiccator until use. Spotting of reagents on ring resonators is highly reproducible between chips.

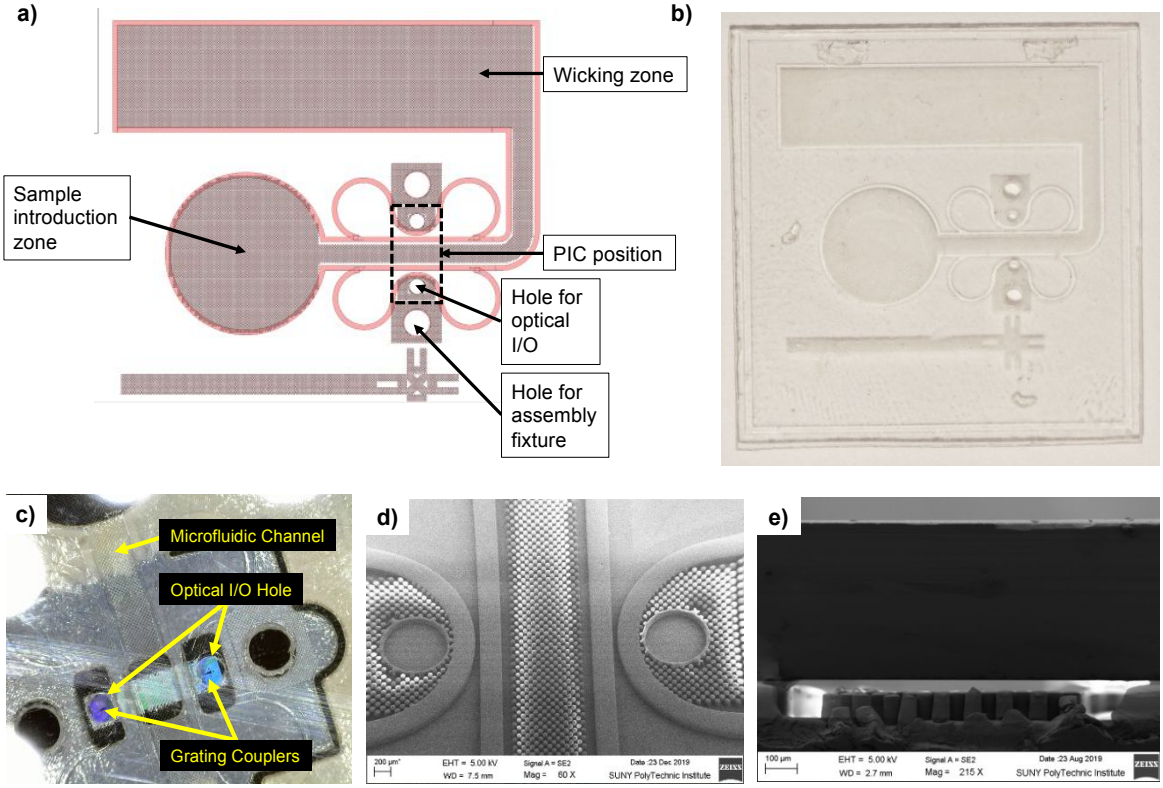

Figure 3: (a) Schematic of the microfluidic card design. (b) Image of a fabricated card; c) Optical microscope image showing a PIC integrated with a fabricated card. Grating couplers on the PIC and optical I/O holes on the card are indicated; d) Scanning electron micrograph (SEM) of the fluidic channel showing pillars near the detection area (attachment point for the PIC); e) cross-section of integrated micropillar microfluidics card showing micropillar height and spacing.

Assay Consumable Assembly

Zeonor micropillar fluidic cards were first treated with oxygen plasma for one minute to increase the hydrophilicity of the fluidic channels (Plasmod Plasma System, Nordson Plasma Systems, Concord, CA). Double-sided, 57-µm-thick adhesive tape (467MP, 3M, St. Paul, MN) was patterned using a laser cutter (Full Spectrum Laser, Hobby Series 20 x 12) to interface the fluidic card with a photonic chip. The adhesive covered the entirety of the micropillar channels, leaving small windows for the photonic gratings to be accessed with optical fiber signals, and for ring resonator sensors to interface with sample flowing through the channel. Additionally, a large inlet hole allowed access with a pipette for sample addition to the sample introduction zone (Figure 3(a)). Patterned adhesive tape was added to the fluidic cards using a custom alignment device, and a strip of filter paper (Q1, Whatman, Little Chalfont, UK) was placed between the micropillar outlet channel and adhesive, to facilitate continuous flow once the channel had filled. Once the adhesive was applied to the fluidic card, photonic chips were manually aligned to the channel and optical-access ports. Figure 3 shows an image of the completed assay consumable (Figure 3(c)), and SEM images of micropillars in the flow channel in the area where the PIC is attached (Figure 3d and 3e).

Apparatus

The assembled assay consumable was aligned to an optical source, which consists of a custom optical element (Syntec Optics, Rochester, NY) that allowed for light to be coupled to and from the photonic grating couplers from below. A schematic of the optical hub testing apparatus is shown in Figure 4. A tunable laser source (Keysight 81606A) is directed through a polarization controller (Thorlabs FPC561 with SMF-28 FC/PC connectors) to obtain linearly polarized light with TE orientation relative to the silicon nitride waveguide. Light is directed though the input of the optical hub and focused on the input grating of the PIC. Output light from the second PIC grating is collected by the optical hub and directed through a multimode fiber (Thorlabs M123L01) to the optical power meter (Keysight N7745A). Alignment of the PIC to the optical hub is facilitated by a dual-camera VIS/IR microscope. A 5x IR objective lens (Mitutoyo Plan Apo NIR 46-402) with on-axis illumination directs light though a long-pass dichroic mirror (Thorlabs DMLP950R) to either the IR camera (WiDy InGaAs 650) or VIS CMOS camera (Thorlabs DCC1645C). Proper alignment is confirmed by IR micrograph.

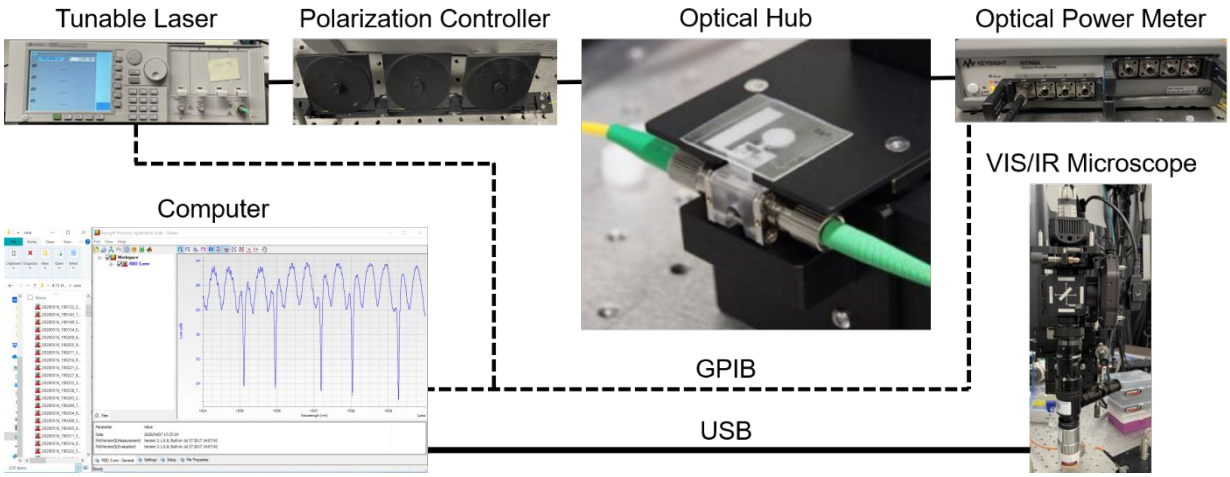

Figure 4: Schematic representation of the optical hub photonic biosensing apparatus. VIS, visible-wavelength light; IR, infrared-wavelength light; GPIB, general purpose interface bus; USB, universal serial bus.

The tunable laser and optical power meter are connected to a computer via General-Purpose Interface Bus (GPIB) and are controlled by the Insertion Loss software of the Keysight Photonic Application Suite (N7700A). Measurements are performed by repeated wavelength scans in the vicinity of resonance signals from the control and probe rings (6 nm scans). The resonance redshift is proportional to the binding of material to the ring surface. Specific shift due to capture of target analyte is calculated by subtracting the redshift of the control ring from that of the probe ring, using a data analysis protocol discussed below.

Spectral Measurements and Sample Addition

Once the device was aligned, 6-nm spectra were taken continuously at 1 pm resolution, generally around 1550 nm, with each spectral measurement taking about 6 seconds. All spectra were automatically saved for analysis. Once a spectrum was acquired after alignment, the experimenter sequentially added samples as follows. First, 20 µL of PNHS, diluted 1:5 in AWB, was added. This step served three purposes: first, to wash off the stabilizer (Stabilcoat) and expose the antigen-functionalized rings; second, to allow the peak from each ring to equilibrate to an environment with a similar bulk refractive index to that of the human serum samples; and third, to block nonspecific binding sites. Once the bolus of sample over the inlet had diminished, but not dried out, the serum sample to be measured was added. As with the PNHS, the sample was diluted 1:5 in AWB. Next, 5 µL of AWB was added to wash away any unbound material and match the bulk refractive index of the next sample. Lastly, 10 µL of goat anti-hIgG antibody (Jackson Immunoresearch, West Grove, PA) at 10 µg/mL was added to selected runs to confirm that the shift seen from the addition of sample was due to anti-RBD or anti-S1+S2 antibodies binding to the resonator.

Analysis of Spectra

Collected spectra were processed automatically through a custom MATLAB (MathWorks, Natick, MA) script to convert the binary Keysight data into comma-separated values (CSV) files to be further analyzed. A Python script was used to analyze spectral features including peak location, peak height, quality factor, chi-squared values and peak fitting parameters. Briefly, data are fit using a defined chi squared minimization in Python package scipy.optimize using the minimize function.[24] Five parameters of a Lorentzian peak function are minimized. The Lorentzian peak function is defined as:

$$L(x) = \frac{c - a}{\left(\frac{b - x}{d}\right)^2 + e}$$

where a is the peak intensity, b is the wavelength at peak maximum, c is the baseline intensity value that dictates peaks or troughs, d defines a full-width at half maximum (FWHM) guess, e defines an extinction ratio value that separates resonances from noise fluctuation, and x represents the array of scanned wavelengths. The chi-squared minimization requires a function to be minimized, initial guess values for Lorentzian parameters, definition of the Lorentzian function and solver selection. Our data minimization is performed using the Powell method which fits data without differentiation.[25]

Spectral peaks are detected by screening intensity values for minima, where the user defines how many minima are expected, and the approximate minima and function waist within the specified wavelength scan range. Chi-squared minimization is used to obtain best fit. Once the best-fit is obtained, spectral characteristics including peak location, peak height, and quality factor are calculated from the best fit data, with chi-squared values indicating the quality of fit.

Results

Characterization of fabricated photonic sensors:

A typical spectrum from fabricated rings is presented in Figure 5(a). Measured quality factors typically exceeded 10^5, with extinction ratios in excess of 27 dB. The intrinsic quality factor of the resonator cavity was calculated to exceed 2 x 10^5.[2] To our knowledge, these are the highest recorded quality factors for silicon nitride ring resonators with an aqueous upper cladding used for biosensing. The measured free spectral range (FSR) was 2.122 nm at 1555 nm vacuum source wavelength. From the intrinsic Q-factor, the ring loss was determined to be 0.35 dB/cm.

Design, testing, and simulation of micropillar microfluidic cards

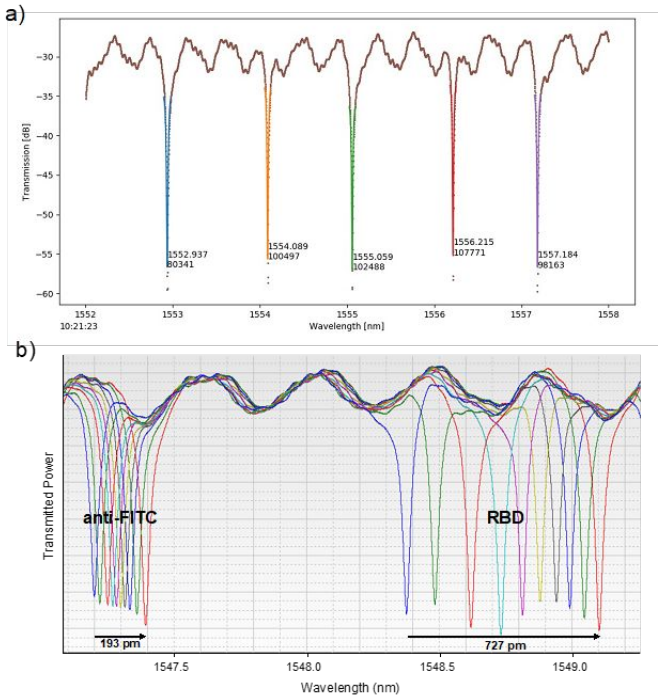

Figure 5. (a) Transmission spectrum with sequential resonances for control and experimental rings with aqueous upper cladding. The control and experimental rings have slightly different radii to separate their transmission spectra. Two free spectral ranges plus one additional peak are shown. Each resonance was fit with a Cauchy-Lorentz function to determine resonance wavelength and quality factors. The fitted wavelength of the resonance (top number, in nm) and quality factor for the fit (lower number) are indicated on the plot. As shown, resonance extinction ratios are in excess of 27 dB, and measured quality factors frequently exceed 10^5, approaching the calculated (designed) intrinsic quality factor near 2 x 10^5. (b) Antibody sensing spectral shifts for an anti-RBD measurement. Each ring has a corresponding resonant wavelength, at which we see a trough in transmitted power. The peaks on the left correspond with the anti-FITC-functionalized ring, while those on the right with the RBD peptide-functionalized ring. With the addition of sample containing anti-RBD antibodies, the right peak shifts as antibodies bind to the ring, while the anti-FITC ring shifts much less, due to nonspecific interactions with serum proteins.

The design of the micropillar microfluidic card was informed by finite element models (COMSOL) of fluid flow. While extensive descriptions of the modeling effort are beyond the scope of this paper, a brief overview of the final micropillar configuration is useful here. Our system is designed such that the card is oriented with the photonic sensor chip mounted upside down, facing the microfluidic channels of the hot-embossed polymeric microfluidic component. To ensure proper sensing, liquid solution with diluted sample must flow uniformly along the microfluidic channel and reach the recessed sensor area (ring resonator in a trench), without forming bubbles. To achieve lateral uniform flow, we first designed and fabricated micropillar microfluidic cards with varying shape, size, and density of micropillar structures under the photonic sensor chip and throughout the microfluidic channels. From our experiments (supplementary videos 1-3), it is evident that without pillars in the sensor area, parabolic flow in at the corners of the fluidic channels dominates, and there is possibility of bubble formation under the sensing area. Hence, we designed uniform micropillar arrays located before and after the sensing area.

To ensure diluted sample reached the sensor well or ring resonator surface we developed a finite element method 3D simulation model in COMSOL Multiphysics. This COMSOL 3D 2-phase microfluidic model was used to simulate aqueous-based sample liquid reaching the recessed sensing surface where the ring resonators are exposed (Figure 6). Symmetry along mid channel was utilized to reduce computational overhead. The micropillar diameter used was 50 µm with a height of 80 µm, and center to center distance between each pillar of 103 µm. Capillary flow in the microfluidic channel was modeled as 2 phase laminar flow with a moving fluid-fluid boundary. Initially the channel was filled with phase $\boldsymbol{\phi = 0}$ air and then simulated until the channel filled with liquid. Figure 6 shows the volume fraction filled by liquid and air in the channel. Blue represents filled with air initially and red represents filled with liquid. This simulation shows uniform capillary flow under the sensor chip and complete filling of the recessed sensor well without bubble formation, supporting our final design.

Measurement of SARS-CoV-2 antibodies in Convalescent Serum Samples

We first validated the completed assay consumables (functionalized sensor PIC plus micropillar microfluidic card) using commercial SARS-CoV-2 antibodies. For monoclonal antibodies raised against SARS-CoV-2 RBD, we achieved total resonance shifts of about 200 pm for an antibody concentration of 10 µg/mL, and about 50 pm for 1 µg/mL (data not shown). Then we tested serum samples of unknown antibody concentrations from convalescent COVID-19 patients in the same manner. Serum samples were obtained from convalescent Covid-19 patients at least 14 days out of active disease. Samples were processed and stored at -80 °C upon receipt and then thawed and diluted as described in the Methods section prior to running the assays.

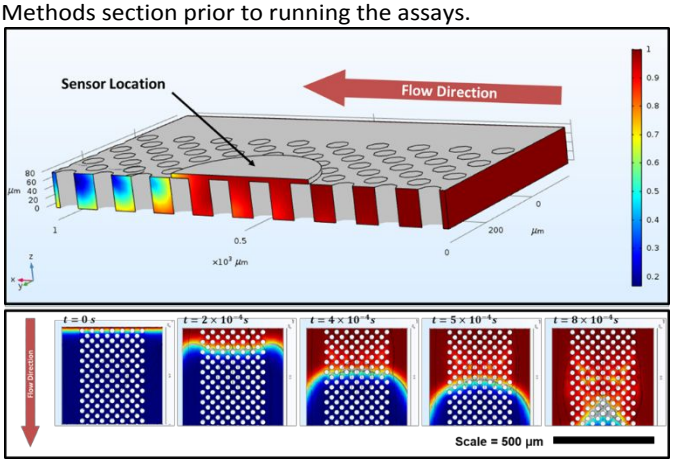

Figure 6. Microfluidic flow simulation performed in COMSOL Multiphysics to illustrate fluid wicking through the hot-embossed, micropillar-filled channels of the micropillar microfluidic card. Top: Simulated wicking of aqueous fluid through the micropillar-filled channel and into the recessed location of the ring-resonator biosensor. The color bar indicates the fluid-filled volume fraction where 0 = empty and 1 = completely filled. Bottom: Simulated wicking of aqueous fluid through the micropillar-filled channels at different time points from 0 to 0.8 milliseconds.

The use of an anti-FITC control ring is important to measure nonspecific binding, as all samples produced non-negligible resonance shifts in these rings. The control ring also corrects for any changes in temperature over the course of the experiment. The response measured in the RBD rings was much higher in all convalescent samples, however. Figure 5b shows

representative spectra for a convalescent COVID-19 patient sample containing a high titer of anti-SARS-CoV-2 antibodies (as measured by ELISA[26]). The anti-FITC ring (represented by the left peak) shifted about 200 pm over the course of ten minutes, while the SARS-CoV-2 RBD-functionalized ring shifted over 700 pm in this time. Similar results were obtained for PICs functionalized with S1+S2 (data not shown).

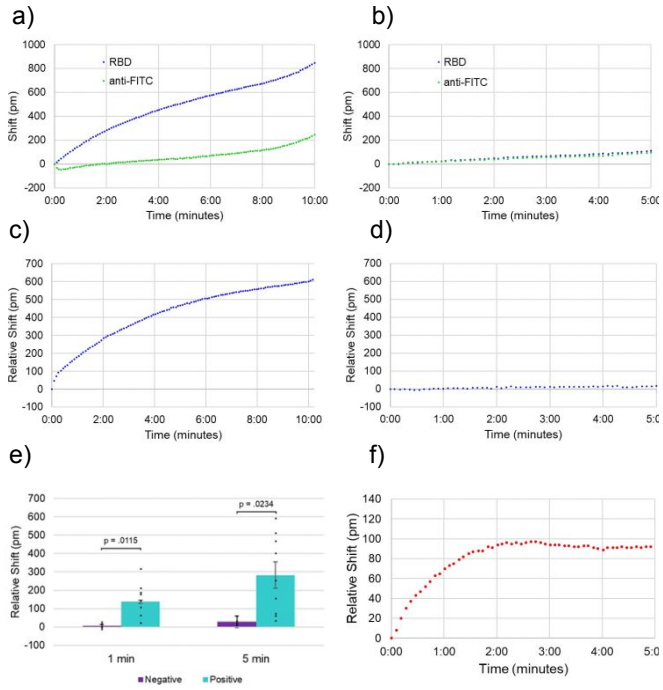

Figure 7. Sample binding curves. (a) and (b) show resonant wavelength shift of control (green) and test (blue) rings over time. (a) corresponds to a convalescent COVID-19 patient serum sample and (b) a negative control. (c) and (d) are the anti-FITC-subtracted response curves corresponding to the same samples. (e) Anti-RBD antibody detection in convalescent COVID-19 patient samples. The photonic sensor platform is able to discriminate between anti-SARS-CoV-2 antibody-positive and -negative samples with good accuracy at the 1-minute (p = 0.0115) and 5-minute (p = 0.0234) timepoints. Sensitivity is 77.8% and specificity is 100%; (f) representative anti-IgG trace for a positive sample showing confirmation of IgG response.

Data were analyzed as described above, with response curves plotted for shifts in both the anti-FITC and RBD or S1+S2 rings over time. Subtraction of the anti-FITC control shift from the experimental (RBD or S1+S2) ring response provided a relative shift binding curve. Figure 7 shows representative binding curves to RBD for both COVID-positive (convalescent) and -negative samples. The response in the positive sample is apparent, with the negative sample showing almost no binding. Notably, a strong, specific signal is observed for the anti-RBD positive sample in a minute or less (Figure 6(a) and (c)).

To compare the response of different samples, we recorded the shift after 1 and 5 minutes for each assay. While the choice of these time points is somewhat arbitrary, we found that these were effective for understanding both the initial response (slope) of the assay and projected maximum shift. As may be seen in the representative data shown in Figure 6, however, signal continues to accumulate in both rings after the 5-minute time point. We were gratified to observe that the platform is able to reliably distinguish positive from negative samples with an assay time of only one minute. As shown in Figure 7(e) we obtained p values of 0.0115 and 0.0234 for 1- and 5-minute measurements, respectively, for discrimination between the two groups. These yield a sensitivity of 77.8% and a specificity of 100%, as there were no false positives.

The results described thus far all represent total antibody (total Ig) in the sample. To discriminate antibody class, it is necessary to incorporate a second step in which a secondary antibody (anti-IgG, -IgM, or -IgA) is flowed over the chip.[27] We tested our ability to detect IgG-specific signals by running some experiments with a second step using an anti-IgG secondary label antibody. As the binding of a secondary antibody to the patient-derived antibodies increases the mass in close proximity to the sensor, this results in an additional resonance shift for the experimental ring. As described earlier, that chip was washed with assay wash buffer, and then 10 µg/mL of anti-IgG in AWB was added. Because the AWB matrix contains no protein other than the label, the resulting binding curve yields an endpoint shift, as shown in the representative curve in Figure 6f. While quantitative anti-IgG response was not rigorously studied here, shifts were generally between 100 and 150 pm. These data demonstrate that the photonic sensor platform can also be used to perform antibody isotype assessment assays to improve understanding about a patient's state of infection.

Analysis of vaccinated subjects

We hypothesized that the disposable photonics platform would also provide a useful method for rapidly profiling individual responses to SARS-CoV-2 vaccination. To test that hypothesis, we examined serum samples from three individuals, taken at several timepoints during the process of vaccination with the Pfizer mRNA vaccine (pre, 1 week post first dose, 2 weeks post first dose, and 1 week post second dose). Responses to SARS-CoV-2 RBD-functionalized sensors are shown in Figure 8. As expected based on clinical trial data,[28] all three subjects produced an anti-RBD response to the vaccine, with shifts 1 week post second dose within the range observed for convalescent COVID-19 patients. Two of the subjects (2 and 3) were observed to have a significant boost in response after their second dose, while Subject 1 had a more modest second dose response. The modest anti-RBD response of subject 1 pre-vaccination suggests prior exposure to SARS-CoV-2, although

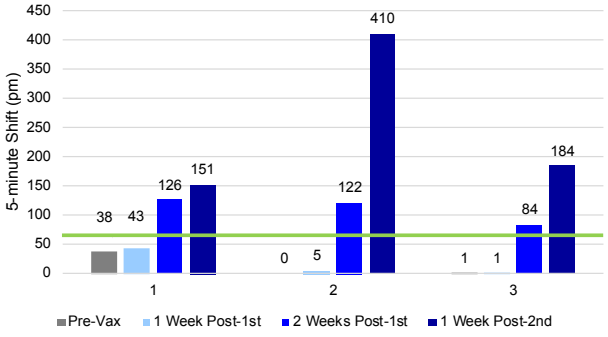

Figure 8. Analysis of three subjects undergoing vaccination with the Pfizer mRNA vaccine for SARS-CoV-2. Serum samples were acquired and tested pre-vaccination, 1 week after the first dose, 2 weeks after the first dose, and 1 week after the second dose. Numbers above each bar indicate the reference (anti-FITC) subtracted shift at 5 minutes. The green line indicates two standard deviations above the mean signal for the negative subjects shown in Figure 7e; signals above this indicate a significant vaccine response.

this person did not report having had active COVID-19 disease at any point.

Conclusions

We have successfully developed an inexpensive silicon photonics sensor platform integrating silicon nitride ring resonator-based biodetection with plastic micropillar microfluidics for sample handling. Ring resonator PICs produced at 300 mm wafer scale using foundry CMOS processes (AIM Photonics) are of high optical quality, and are able to provide state-of-the-art biosensing performance when combined with the micropillar microfluidics system. Sensors functionalized with SARS-CoV-2 antigens (RBD and S1+S2 ECD, domains from the virus' spike protein) are able to detect and quantify antibody responses in human serum samples from both convalescent COVID-19 patients and vaccinated subjects.

Of particular note is the speed with which these assays can be performed. With this platform, a patient's antibody status, and thus ideally immunity status, can be obtained within minutes, following serum separation. Positive vs. negative discrimination is achieved with p values of 0.0234 at five minutes and 0.0115 within just one minute. Preliminary data using samples from vaccinated subjects confirms the utility of the platform for assessing vaccine response. This will have substantial utility for assessing the performance of the vaccine in different patient groups, and for studying the length of time that anti-SARS-CoV-2 antibodies persist in vaccinated subjects. Studies along these lines are currently in progress in our laboratories. While small, the 1 x 4 mm sensor PIC has sufficient real estate to permit development of multiplex assays; these could in principle be used to report on antibody responses to SARS-CoV-2 mutants. By keeping the overall sensor format small, we anticipate that this will reduce cost to the point that photonic sensors become viable components of high-volume clinical assay consumables.

Author Contributions

Conceptualization: RJ, HW, NCC, BLM; Funding acquisition: BLM, RJ, HW, NCC, CM; Methodology: JSC, DJS, MA, MRB, RJ, HW, NCC, CM, BLM; Investigation: JSC, DJS, MA, MRB, CS, NT, EY, AMK, AZ, NJ, BP; Writing – original draft: JSC, DJS, MA, MRB, AZ, CM, NCC, BLM: Writing – review & editing: JSC, DJS, MRB, RJ, HW, NCC, BLM.

Conflicts of interest

JSC, DJS, MA, MRB, NT, RJ, HW, NCC, and BLM are co-inventors on a patent application relating to the work described in this manuscript.

Acknowledgements

This work was supported by the U.S. Department of Defense under AIM Photonics, Air Force Contract FA8650-15-2-5220. The views and opinions expressed in this paper are those of the authors and do not reflect the official policy or position of the United States Air Force, Department of Defense, or the U.S. Government.

Notes and references

1. M. Cornelissen, and J. Huskens, *ACS Appl. Bio Mater.*, 2020, **3**, 4566-4572.
2. B. J. Luff, J. S. Wilkinson, J. Piehler U. Hollenbach, J. Ingenhoff, and N. Fabricius, *J Lighwave Tech*, 1998, **16**, 583-592.
3. M. S. Luchansky, A. L. Washburn, M. S. McClellan, and R. C. Bailey *Lab Chip*, 2011, **11**, 2042-2044.
4. M. C. Cardenosa-Rubio, H. M. Robison, and R. C. Bailey *Curr Opin Env Sci Health*, 2019, **10**, 38-46.
5. J. E. Baker, R. Sriram, and B. L. Miller, *Lab Chip*, 2017, **17**, 1570-1577.
6. J. E. Baker, R. Sriram, and B. L. Miller, *Lab Chip*, 2015, **15**, 971–990.
7. Y. Zhuo and B. T. Cunningham, *Sensors*, 2015, **15**, 21613-21635.
8. S. Chakravarty, W.-C. Lai, Y. Zou, H. A. Drabkin, . M. Gemmill, G. R. Simon, S. H. Chin, and R. T. Chen, *Biosens Bioelectron*, 2013, **43**, 50-55.
9. E. Luan, H. Shoman, D. M. Ratner, K. C. Cheung, and L. Chrostowski, *Sensors*, 2018, **18**, 3519.
10. Y. Galipeau, M. Greig, G. Liu, M. Driedger, and M.-A. Langlois, *Front Immunol*, 2020, **11**, 610688.
11. D. Sterlin, A. Mathian, M. Makoto, A. Mohr, et al., *Sci Trans Med*, 2021, **13**, eabd2223.
12. S. Kerman, D. Vercruysse, R. Claes, A. Stassen, M. Hasan, R. Neutens, V. Mukund, N. Verellen, X. Rottenberg, L. Lagae, and P. Dorpe, *ACS Photon*, 2017, **4**, 1937-1944.
13. C. J. Oton, *IEEE Phtonics J*, 2016, **8**, 2700208.
14. N. M. Fahrenkopf, C. McDonough, G. L. Leake, Z. Su, E. Timurdogan, and D. D. Coolbaugh, *IEEE J. Selected Top Quant Electron*, 2019, **25**, 1-6.
15. R. S. Hale, R. T. Bonnecaze, and C. H. Hidrovo, *Int J Multiphase Flow*, 2014, **58**, 39-51.
16. D. Stoecklein, C.-Y. Wu, D. Kim, D. Di Carlo, and B. Ganapathysubramanian, *Phys Fluids*, 2016, **28**, 012003.
17. C. Ishino, M. Reyssat, E. Reyssat, K. Okumura, and D. Quére, *EPL*, 2007, **79**, 56005
18. R. Xiao, R. Enright, and E. N. Wang, *Langmuir*, 2010, **26**, 15070-15075.
19. W.-X. Chen, J.-G. Li, X.-H. Wan, X.-S. Zou, S.-Y. Qi, Y.-Q. Zhang, Q.-M. Weng, J.-Y. Li, W.-M. Xiong, C., and W.-L. Cheng, *Oncol Lett*, 2019, **17**, 1581-1588.
20. J. Hansson, H. Yasuga, T. Harldsson, and W. van der Wijngaart, *Lab Chip*, 2016, **16**, 298-304.
21. N. S. K. Gunda, J. Joseph, A. Tamayol, M. Akbari, and S. K. Mitra, *Microfluid Nanofluid*, 2013, **14**, 711-721.
22. Z. Ding and E. R. Scalice, WO2014078679A1.
23. Z. Ding, P. C. Hosmier, E. R. Scalice, D. P. Salotto, and D. A. Heavner, US10073091B2.
24. P. Virtanen, R. Gommers, T. E. Oliphant, M. Haberland, T. Reddy, D. Cournapeu, E. Burovski, P. Peterson, W. Weckesser, J. Bright, S. J. van der Walt, M. Brett, J. Wilson, K. J. Millman, N. Mayorov, arey, I. Polat, Y. Feng, E. W. Moore, J. VanderPlas, D. Laxalde, J. perktold, R. Cimrman, I. Henriksen, E. A. Quintero, C. R. Harris, A. M. Archibald, A. H. Riberiro, F. Pedregosa, P. van Mulbregt, and SciPy 1.0 Contributors, *Nature Methods*, 2020, **17**, 261-272.
25. M. J. D. Powell, *Computer J*, 1964, **7**, 155-162.
26. D. J. Steiner, J. S. Cognetti, E. P. Luta, A. M. Klose, J. Bucukovski, M. R. Bryan, J. J. Schmuke, P. Nguyen-Contant, M. Y. Sangster, D. J.

Topham, and B. L. Miller, *Biosens Bioelectron*, 2020, **169**, 112643.
27. Q. Long, B. Liu, H. Deng, et al., *Nat Med*, 2020, **26**, 845-848.
28. M. J. Mulligan, K. E. Lyke, N. Kitchin, J. Absalon, et al., *Nature*, 2020, **586**, 589-593.